

AUTHOR QUERIES

AUTHOR PLEASE ANSWER ALL QUERIES

PLEASE NOTE: Please note that we cannot accept new source files as corrections for your article. If possible, please annotate the PDF proof we have sent you with your corrections and upload it via the Author Gateway. Alternatively, you may send us your corrections in list format. You may also upload revised graphics via the Author Gateway.

Carefully check the page proofs (and coordinate with all authors); additional changes or updates WILL NOT be accepted after the article is published online/print in its final form. Please check author names and affiliations, funding, as well as the overall article for any errors prior to sending in your author proof corrections. Your article has been peer reviewed, accepted as final, and sent in to IEEE. No text changes have been made to the main part of the article as dictated by the editorial level of service for your publication.

AQ:1 = Please confirm whether the edits made in the current affiliation of all the authors are correct.

AQ:2 = Please provide the city and postal code for Kyoto University.

AQ:3 = Please confirm or add details for any funding or financial support for the research of this article.

AQ:4 = If you haven't done so already, please make sure you have submitted a graphical abstract for your paper. The GA should be a current figure or image from your accepted article. The GA will be displayed on your articles abstract page on IEEE Xplore. Please choose a current figure from the paper and supply a caption at your earliest convenience for the graphical abstract. Note that captions cannot exceed 1800 characters (including spaces). If you submitted a video as your graphical abstract, please make sure there is an overlay image and caption. Overlay images are usually a screenshot of your video that best represents the video. This is for readers who may not have access to video-viewing software. Please see an example in the link below: <http://ieeeaccess.ieee.org/submitting-an-article/>

Received 10 December 2025, accepted 17 January 2026. Date of publication 00 xxxx 0000, date of current version 00 xxxx 0000.

Digital Object Identifier 10.1109/ACCESS.2026.3656449

MTSCCleav: A Multivariate Time Series Classification (MTSC)-Based Method for Predicting Human Dicer Cleavage Sites

COLEMAN YU^{ID}¹, RAYMOND CHI-WING WONG^{ID}²,
AND TATSUYA AKUTSU^{ID}¹, (Senior Member, IEEE)

Bioinformatics Center, Institute for Chemical Research, Kyoto

¹Bioinformatics Center, Institute for Chemical Research, Kyoto University, Japan

²Department of Computer Science and Engineering, The Hong Kong University of Science and Technology, Hong Kong

Corresponding author: Coleman Yu (cyy@kuicr.kyoto-u.ac.jp)

The work of Tatsuya Akutsu was supported in part by Japan Society for the Promotion of Science (JSPS), Japan, under Grant 22H00532 and Grant 22K19830.

ABSTRACT MicroRNAs (miRNAs) are small non-coding RNAs (ncRNAs) that regulate gene expression at the post-transcriptional level, thereby playing essential roles in diverse biological processes. The biogenesis of miRNAs requires Dicer to cleave at specific sites on the precursor miRNAs (pre-miRNAs). Several machine learning approaches have been proposed to predict whether an input sequence contains a cleavage site. However, they rely heavily on complex feature engineering or opaque deep neural networks. It results in a lack of generalizability and a long running time. There is a need for an alternative modeling paradigm that is accurate, fast, and simple. We propose an approach to frame the task as a multivariate time series classification problem. Nine encoding methods have been proposed to convert the RNA sequence into a time series. The predicted secondary structure is also converted to a time series. We also leverage the probabilities of the base pairs in the predicted secondary structure. Computational experiments demonstrate that our proposed method can achieve better or comparable results in terms of using a simpler, more intuitive model and less computational time. It achieves 3.7X to 28.8X speedup. Through perturbation experiments, we found that regions close to the center of pre-miRNAs are essential for predicting human Dicer cleavage sites. By transforming the RNA sequence and its secondary structure information into a multivariate time series and utilizing simple, state-of-the-art time series classifiers, we achieved comparable or even superior performance in a simpler and faster manner. Code is available at: <https://github.com/colemanyu/time-series-classification-cleavage>

INDEX TERMS miRNA, dicer cleavage site, genomic signal processing (GSP), multivariate time series classification (MTSC, TSC).

I. BACKGROUND

One of the most important theories in molecular biology is the central dogma. It depicts the flow of genetic information [1], [2]. Proteins are the functional units. The information stored in DNA is used to create them. Genes (segments) in DNA are used as templates for messenger RNAs (mRNAs) synthesis. An mRNA acts as a set of instructions to assemble a chain of amino acids, which form a linear polypeptide.

The associate editor coordinating the review of this manuscript and approving it for publication was Vincenzo Conti^{ID}.

To become biologically active, this chain is folded into a specific 3D structure, a proper configuration that enables it to perform its desired functions. This folded polypeptide is called a functional protein, or simply a protein. This entire process closely resembles how a computer program runs on a machine. The source code does not function by itself. First, it is translated into an assembly code (a lower-level, less human-readable form) and then into an executable file that can actually perform the intended tasks [3].

These mRNAs are called “coding RNAs” because they code for proteins. There are other genes in which the

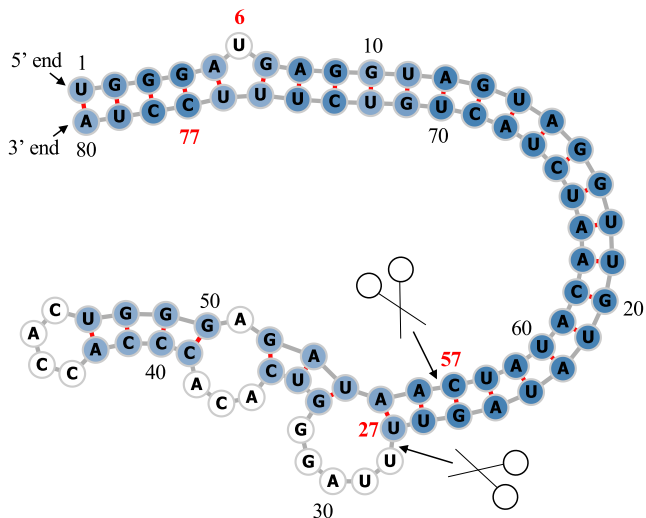


FIGURE 1. Predicted secondary structure of the sequence S of pri-miRNA “hsa-let-7a-1”². Experimental evidence suggests that the two deviated mature miRNAs are UGA . . . GUU and CUA . . . UUC. They are S(6 : 27) and S(57 : 77) (Both ends are inclusive.). The ends are highlighted in bold. Since S(6 : 27) (S(57 : 77)) is near the 5’ (3’) end, we call it “5p (3p) mature miRNA”. The two scissors indicate the two cleavage sites. The color intensity of the nodes reflects their base-pair probability in this predicted secondary structure. The deeper the color, the higher the probability. The unpaired nodes are uncolored. The raw figure is generated by RNAfold web server.³

final product is the RNA molecule itself. They are called non-coding RNAs (ncRNAs). Two types of small ncRNAs are particularly important. They are microRNAs (miRNAs) and small interfering RNAs (siRNAs). Their discovery was recognized with the 2006 Nobel Prize in Physiology or Medicine,¹ awarded for work completed only eight years prior [1].

In this study, we focus on miRNAs. An miRNA can regulate the expression of several proteins. Hence, understanding the biogenesis of miRNAs is of great value. It involves the processing of primary miRNAs (pri-miRNAs). RNAs are 3D molecules. While the 1D sequence of these molecules can be easily obtained by sequencing, it is hard to measure the 3D structure (tertiary structure) from the experiment and predict it directly from the 1D sequence. Many relevant properties of the 3D structure are typically investigated by analyzing the 1D sequence and the predicted 2D structure derived from it, known as secondary structure.

The sequence and its predicted secondary structure of a pri-miRNA “hsa-let-7a-1” is shown in Figure 1.

Recall that a pri-miRNA contains a hairpin loop, also called a stem loop. A microprocessor complex comprising Drosa and DCGR8 cleaves the pri-miRNA to form

a precursor miRNA (pre-miRNA) inside the nucleus. The stem-loop is still preserved, but the two arms become shorter. After that, the pri-miRNA is transported by Exportin 5 from the nucleus to the cytoplasm. It is further cleaved by an enzyme called Dicer [4]. Dicer cleaves the stem-loop from the two arms at the two cleavage sites, shown as the two scissors in Figure 1. The stem-loop is removed. It results in a short double-stranded miRNA molecule, known as an miRNA duplex, which consists of the 5p strand and the 3p strand.⁴ These molecules may be subjected to additional trimming. The miRNA duplex is loaded into an RNA-induced silencing complex (RISC). RISC unwinds the duplex and tends to retain the strand with the less stable 5’ end as the guide strand. The other strand is called the passenger strand. The retained strand guides the RISC to silence the target mRNA. Note that both strands can become the guide strand.

Dicer plays an important role in the biogenesis of miRNAs. It is reasonable to argue that the structure of the pre-miRNAs informs Dicer about the cleavage process. It would be of great benefit to understand how Dicer selects cleavage sites from the neighborhood information near the cleavage sites. Studies [5], [6], [7] revealed that the secondary structures are essential for cleavage site determination. Hence, to predict or classify whether a subsequence, extracted from the sequence of a pri-miRNA, contains a cleavage site, we can make use of both the sequence and secondary structure information. PHDcleav employed support vector machines (SVM), leveraging sequence and structure-based features for the classification [8]. LBSIZEcleav improved upon it by considering the loop and bulge lengths [9]. Reference [10] proposed an ensemble learning approach, using a gradient boosting machine for better accuracy. Reference [11] developed a deep learning model, namely DiCleave. This model used an autoencoder to learn the secondary structure embeddings of pre-miRNAs from all the species in the miRBase database and leveraged this information. All these methods begin with curated pre-miRNA sequences from the miRBase database. Their secondary structures are predicted. Patterns are extracted from the sequence and the secondary structure. They create the positive cleavage patterns by setting the cleavage sites at the middle of the patterns. The follow-up work of [11], which created the cleavage pattern by allowing cleavage sites to appear at any position within the pattern, instead of the middle only [12]. It created a much larger dataset. This increased dataset facilitates the learning of the deep learning method at the cost of increased running time. We utilized the original dataset setting [8], [9], [10], [11]. DiCleave is the current state-of-the-art (SOTA) for this problem with the original dataset setting.

These models suffer several limitations. They rely heavily on complicated feature engineering or opaque deep learning models [10], [11], [12]. It results in a lack of generalizability

¹The Nobel Prize in Physiology or Medicine 2006 - NobelPrize.org: <https://www.nobelprize.org/prizes/medicine/2006/summary/> (Accessed on: 2025-06-13).

²Its miRBase entry: <https://mirbase.org/hairpin/MI0000060>. (Accessed on: 2025-06-12).

³RNAfold web server: <http://rna.tbi.univie.ac.at/cgi-bin/RNAWebSuite/RNAfold.cgi>. (Accessed on: 2025-06-12). The figure is viewed in “forna”. This view option can be chosen on the website.

⁴The 5p strand comes from the 5’ arm while the 3p strand comes from the 3’ arm. For the directionality, the 5p (3p) strand retains the original 5’ (3’) end of the pre-miRNA.

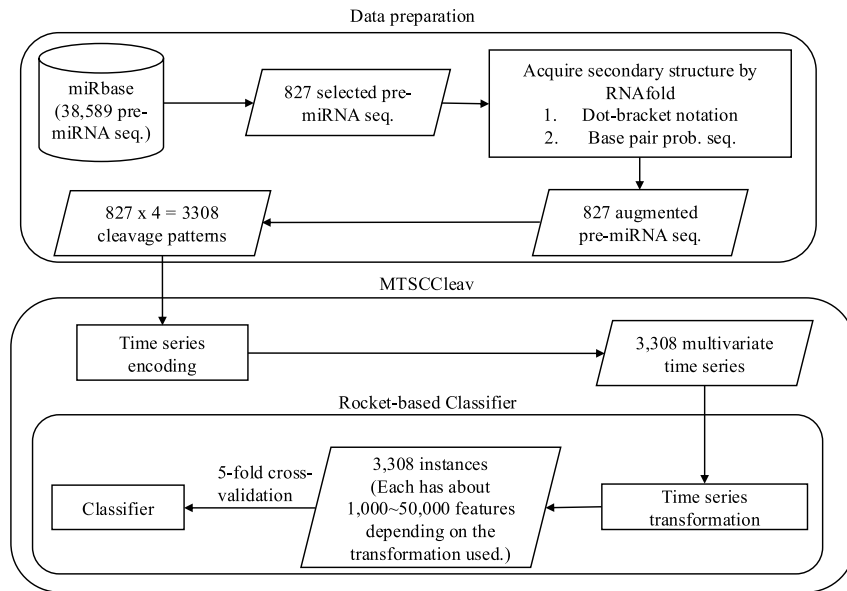


FIGURE 2. The overall pipeline of this study. Symbol notations: cylinder - dataset, rectangle - process, parallelogram - input / output rounded rectangle - component.

and a long running time. There is a need to design a simpler model so that it can be easily extended to other prediction tasks on RNA data. One way to analyze sequence data is to transform it into time series data. In response to this, we proposed a multivariate time series classification-based method to provide a simpler, more computationally efficient framework for this task. Our contributions are shown as follows.

- 1) To the best of our knowledge, we are the first to frame the prediction of the cleavage sites as a multivariate time series classification problem.
- 2) We introduced nine encoding methods to convert RNA sequences to time series.
- 3) We proposed utilizing the base-pair probabilities in the predicted secondary structure for the prediction. To our surprise, this information has been ignored in the existing studies.
- 4) For computational efficiency, our method achieves a 3.7X to 28.8X speedup compared to the state-of-the-art (SOTA).
- 5) We conducted perturbation-based experiments. It shows that regions close to the cleavage sites are important for this problem. It is consistent with the existing study [10].

II. METHODS

The overall pipeline of this study is summarized in Figure 2.

A. DATA PREPARATION

We used miRBase database [13].⁵ The database comprises miRNA data from various organisms [14]. The database contains 38,589 miRNA records. Each record refers

to an miRNA sequence, along with other properties such as name, accession, organism, and information on its derivative miRNA products. We are interested in pri-miRNA in humans. The derivative miRNA products are the mature miRNAs. The database also annotates the location of the mature miRNA within the original sequence and indicates whether its existence has experimental evidence.

Table 1 shows its four representative records. We first selected the records from humans (*Homo sapiens*). It resulted in 1,917 records. To identify the actual locations of the two cleavage sites in the pri-miRNA sequence supported by experimental evidence, we selected records that have two mature miRNAs resulting from cleavage at the 5p arm and the 3p arm, both of which have experimental support. Hence, only “MI0000060” (“hsa-let-7a-1”) would be selected in the table. It would serve as our running example. Its whole sequence is listed in Table 2. Based on the filtering criterion (i.e., from *Homo sapiens* and having experimental supports), we selected 827 experimentally validated pre-miRNA sequences, each with its two mature miRNA products. This formed our dataset.

1) AUGMENT THE DATASET WITH SECONDARY STRUCTURE INFORMATION

We leveraged the predicted secondary structure of these sequences to enhance the accuracy of the classification. Recall that a specific three-dimensional (3D) structure is required for DNA, RNA, and protein to perform functions [15]. However, finding these 3D structures using experimental methods such as X-ray crystallography or nuclear magnetic resonance (NMR) is costly and time-consuming. Hence, prediction methods for such 3D structures are necessary and helpful for downstream analysis. However, predicting the 3D structures is challenging. One of the

⁵The website is www.mirbase.org, and the newest version of the database is Release 22.1 (Accessed on 2025-06-22).

TABLE 1. Selected representative records from miRBase. For the last two columns, the first line shows the name, the second line shows its location in the original sequence, and the third line indicates whether its existence has experimental evidence. The selected one is highlighted in bold.

Accession	Name	Organism	Sequence	Mature miRNA 1	Mature miRNA 2
MI0000001	cel-let-7	Caenorhabditis elegans	<i>UACAC</i> ... <i>UUCGA</i>	cel-let-7-5p 17:38 experimental	cel-let-7-3p 60:81 experimental
MI0000060	hsa-let-7a-1	Homo sapiens	<i>UGGGA</i> ... <i>UCCUA</i>	hsa-let-7a-5p 6:27 experimental	hsa-let-7a-3p 57:77 experimental
MI0000114	hsa-mir-107	Homo sapiens	<i>CUCUC</i> ... <i>ACAGA</i>	hsa-miR-107 50:72 experimental	NA
MI0000238	hsa-mir-196a-1	Homo sapiens	<i>GUGAA</i> ... <i>UUCAC</i>	hsa-miR-196a-5p 7:28 experimental	hsa-miR-196a-1-3p 45:65 not experimental

177 reasons is that there are some “nonconventional” base-pair
 178 interactions (e.g., noncanonical and rare A-G) that allow an
 179 RNA sequence to fold into a 3D structure, in addition to
 180 the (G, U) wobble pair, which is common and functionally
 181 important in RNA secondary structures. It makes the search
 182 space for prediction much larger than, in the 2D case, the
 183 secondary structure. The local structures of the 3D structures,
 184 the secondary structures, only focus on the conventional base-
 185 pair interactions [2]. Hence, predicting secondary structures
 186 is easier and faster. We employed RNAfold from the
 187 ViennaRNA Package⁶ to predict the secondary structure for
 188 a given pri-miRNA S [16]. RNAfold returns the secondary
 189 structure in the dot-bracket notation and a matrix of base-
 190 pair probabilities. The matrix is a square pairwise matrix with
 191 the side length $|S|$, where each entry m_{ij} is the probability
 192 of base s_i paired up with base s_j . Dot-bracket notation is
 193 a way of representing the secondary structure of S . Open
 194 parentheses “(“ (Close parentheses “)”) indicates that the
 195 base is paired with a complementary base further (earlier)
 196 along in S . Dot “.” indicates that the base is unpaired.
 197 Equipped with the matrix, we can construct the base-pair
 198 probability sequence of S . The predicted secondary structure
 199 and the base-pair probability sequence of our running
 200 example are shown in Table 2.

2) EXTRACT CLEAVAGE PATTERNS

201 The locations of the two mature miRNAs on the whole
 202 sequence indicate the probable locations of the two cleavage
 203 sites. The 5p cleavage site must be beyond and near the ending
 204 location of the 5p mature miRNA. We deemed the immediate
 205 bond next to the 5p mature miRNA’s ending position the
 206 5p cleavage site, with the knowledge that the actual cleavage
 207 site may not be this immediate bond but rather the nearby
 208 bonds after it. The same applies to the 3p cleavage site. It is
 209 located at the immediate bond before the starting position of
 210 the 3p mature miRNA.

211 For each arm of each whole sequence, we extracted a
 212 14-string⁷ with the cleavage site located at the center of
 213 the string. The first 7 nt (nucleotide) before the center

⁶The latest stable release is Version 2.7.0 (Accessed on 2025-06-22).

⁷String with length = 14.

215 are highlighted in **bold**. In our running example, it would
 216 be “**UAUAGUUUAGGGU**” for the 5p cleavage site and “**GAGAUACAUAC**” for the 3p cleavage site.
 217 We refer to these 14-strings as cleavage patterns. We also
 218 generate non-cleavage patterns by selecting a 14-string with
 219 the center 6 nt away from the corresponding cleavage
 220 sites towards the corresponding mature miRNA [9], [10]
 221 for each arm of each whole sequence. So, in our run-
 222 ning example, the 5p non-cleavage pattern would be
 223 “**AGGUUGUAUAGUUU**”. The 3p non-cleavage pattern
 224 would be “**ACUAUACAAUCUAC**”.

225 In conclusion, for a given pri-miRNA sequence, we can
 226 generate two cleavage patterns and two non-cleavage pat-
 227 terns. We call these four patterns simply the “four strings”
 228 of a given pri-miRNA. We also call each string a strand. The
 229 “four strings” of our running example are listed in Table 3.

230 We can construct the complementary strand of each of the
 231 strands in the “four strings” by finding the corresponding
 232 paired base for each of the bases in the input strand by
 233 considering the secondary structure information. We use “_”
 234 to denote the unpaired base in the complementary strand. For
 235 example, in Figure 1, “UUAGG” in the 5p cleavage pattern
 236 is unpaired, while other bases pair with some bases, the
 237 resulting complementary strand is “AUAUCAA____UA”.
 238 There is a loop/budge there. We refer to the “four strings”
 239 and the four complementary strands together as the “eight
 240 strings” of the input pre-miRNA. It is also shown in Table 3.

B. TIME SERIES ENCODING

241 A time series $T = t_1, t_2, \dots, t_n$ is a sequence of real-
 242 valued numbers.⁸ A short contiguous region of T is called
 243 a subsequence. A subsequence $T(i:j) = t_i, t_{i+1}, \dots, t_j$ of a
 244 time series T is a shorter time series that starts from position i
 245 and ends at position j , where $i < j$.

246 Strings and time series are temporal sequences. The
 247 difference between strings and time series lies in their
 248 behavioral attributes [17]. For strings, an entry is a
 249 letter from a predefined set called the *alphabet*. For
 250 example, the alphabet is {A, C, G, T} in the DNA string,

⁸Unless otherwise specified, we denote entries of a time series (e.g., T) using the corresponding lowercase letter (e.g., t).

TABLE 2. The whole sequence of “hsa-let-7a-1” and its predicted secondary structure by RNAfold. The corresponding positions of the two mature miRNAs and the probability of the unpaired “U” are highlighted in bold.

Sequence	Secondary Structure (In Dot-bracket notation)
1 UGGGA UGAGGUAGUAGGUUGUAUAGUU 27 28 UUAGGGUCACACCCACCACUGGGAGAU 54 55 AA CUAUACAACUACUGCUUUC CUA 80	1 (((((.(((((((((((((27 28 UUAGGGUCACACCCACCACUGGGAGAU 54 55))))))))))))))))) 80
Base-pair probabilities sequence (the first 10 bases)	
1 (0.549, 0.946, 0.987, 0.987, 0.904) 5 6 (0.000 , 0.841, 0.974, 0.981, 0.890) 10	

253 while $\{A, C, G, U\}$ in the RNA string. For time series,
 254 an entry is a real number. Unlike real numbers, there is
 255 no ordering in the alphabet unless some external domain
 256 knowledge is introduced.

257 The study of applying signal processing techniques
 258 to genomic data is called “Genomic Signal Processing”
 259 (GSP) [18], [19]. In the field of GSP, the time series
 260 representations of DNA strings are referred to as DNA
 261 numeric representations (DNR). Many DNRs have been
 262 proposed. We noted that DNA strings and RNA strings
 263 are equivalent from a computational standpoint. Many
 264 transformation methods designed for DNA can be applied
 265 to RNA by simply substituting T with U . We present nine
 266 encoding methods. The relationship among them is shown
 267 in Figure 3.

268 1) SINGLE VALUE VERSUS CUMULATIVE

269 One of the simple, if not the simplest, encoding is to map
 270 the letters into numbers. Domain knowledge can be utilized.
 271 This approach is called the “Single value mapping” [18],
 272 [20], [21], [22], [23]. One single value is assigned to
 273 each of the letters. Reference [24] employed the atomic
 274 number of each nucleotide as the transformed values, where
 275 $\{G = 78, A = 70, C = 58, T = 66\}$. Reference [25] used
 276 electron-ion interaction potential representation (EIIP) as
 277 such value, where $\{G = 0.0806, A = 0.1260, C = 0.1340,$
 278 $T = 0.1335\}$. Our goal is to transform the input strand and its
 279 complementary strand into time series, aiming to capture the
 280 information contained in these sequences and the secondary
 281 structure implied by them. We employed the following
 282 reasoning to assign the value:

- 283 1) We employ the complementary property [22], [26]
 284 during encoding. Recall that in the base-pairing rules,
 285 G pairs with C to form three hydrogen bonds while A
 286 pairs with U^9 to form two hydrogen bonds. $G-C$ pairs
 287 are more stable than $A-U$ pairs. G (U) can be regarded
 288 as the “inverse” of C (A). We can preserve these base-
 289 pairing rules in the encoding by assigning G (A) and
 290 C (U) opposite values.
 291 2) G and A have a two-ring structure. They are
 292 purines. C and U have a single-ring structure.

⁹In DNA, A pairs with T .

They are pyrimidines. Hence, we put G and A
 293 (C and U) on the same side of the number line with
 294 zero in the middle.

- 295 3) The lower stability of $A-U$ pairs promotes strand
 296 separation, thereby facilitating the unwinding of the
 297 miRNA duplex during RISC loading. Regions rich in A
 298 and U are thus more likely to undergo strand selection
 299 and cleavage events. We assigned A (U) with a larger
 300 absolute value than G (C) to reflect this functional
 301 relevance. It aims to highlight sequence regions with
 302 higher cleavage potential.

303 It results in our baseline transformation method, namely
 304 “Single value mapping” as shown in row 1 of Table 4. S is the
 305 input strand. Note that there are advanced encoding methods
 306 that consider specific values of the assignment to better
 307 encode the nucleotide relationship. Here, we present the
 308 general approach of the mapping and focus on preserving the
 309 complementary property. When we encode S without incor-
 310 porating the corresponding base-pair probability sequence P ,
 311 we set $p_i = 1$ for all the entries of P . We use the first ten
 312 nucleotides of the complementary strand of the 3p cleav of
 313 “hsa-let-7a-1”, as shown in Table 3 as S in the examples
 314 in Table 4.

315 With the assigned value to each nucleotide defined in
 316 single-value mapping, we can compute a cumulative sum
 317 of those values over time. It captures the aggregated signal
 318 by accumulating past events, allowing us to focus on the
 319 trend [27], [28]. We named this method as “Cumulative
 320 mapping”, shown in row 4 of Table 4.

322 2) GROUPED VARIABLE-LENGTH CHANNEL VERSUS 323 GROUPED LOCAL-LENGTH CHANNEL

324 We can transform the input strand into a multivariate time
 325 series with two channels using grouped binary encoding,
 326 where nucleotides are grouped into (A, U) and (G, C) .
 327 It releases our third assumption that A (U) has a larger
 328 absolute value than G (C). We proposed two variations. The
 329 first one allows the output to be variable-length sequences
 330 per channel, depending on group-specific occurrences. The
 331 second one always returns two resulting sequences of a fixed
 332 length. Two variations extended from single value mapping
 333 are shown in rows 2 and 3, while those extended from
 334 cumulative mapping are shown in rows 5 and 6 in Table 4.

TABLE 3. The first row shows the “four strings” of “hsa-let-7a-1”. Their complementary strands are shown in the second row. As a whole, they are referred to as the “eight strings”.

	5p cleav	5p non-cleav	3p cleav	3p non-cleav
Input strand	UUAUGUUUUAGGGU	AGGUUGUAUAGUUU	GAGAUACAUUACA	ACUAUACAAUCUAC
Complementary strand	AUAUCAA_____UA	UCUAACAUUAUCAA_	C_CUGUUGAUUAUGU	UGAUUAUGUUGGAUG

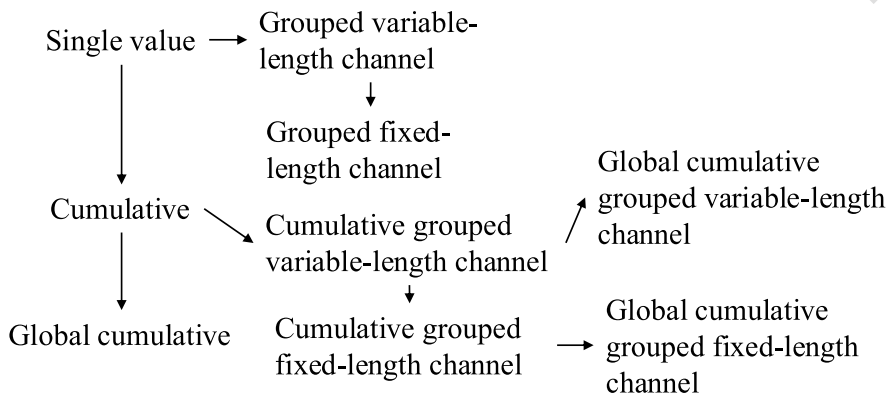


FIGURE 3. Relationship of the proposed encoding methods.

3) GLOBAL CUMULATIVE VERSUS LOCAL CUMULATIVE

In cumulative mapping and its variations, we can choose where to start the accumulation. For a given subsequence S' of the whole sequence S , accumulation can start from the beginning of S even if only S' is used downstream. It can also begin just at the start of the S' . The first one preserves the global context. It can be useful when previous nucleotides (those before S') influence later interpretation. The second one focuses solely on local history in S' , ignoring global history. It is helpful if the previous nucleotides do not affect the chemical property of S' .

Consider $T = 0, -1, \dots, -6$ of the input string S in “Cumulative mapping” in Table 4, which accumulates from 0. S is the suffix with length = 10 of the constructed complementary strand of $S(1 : 63)$ in Figure 1. If we start the accumulation from the first entry of the constructed complementary strand instead, it will yield a different result. Suppose that the last entry of the time series encoded in the cumulative mapping of the constructed complementary strand is -8 , the time series encoded in the “Global cumulative mapping” for S would accumulate from -8 instead of 0. The result is $T = -8, -9, \dots, -14$. Note that it has the same trend as the original T . This “Global cumulative” concept can be applied to every cumulative-based method, as shown in Figure 3.

4) INCORPORATING BASE-PAIR PROBABILITIES

We can incorporate the base-pair probabilities P in the encoding by thinking of it as the weight or confidence p_i in the value assignment of each nucleotide s_i . It is implemented by multiplying the base-pair probability p_i of the nucleotide s_i with the assigned value of the kind of nucleotide of s_i during encoding, as shown in Table 4.

5) TRANSFORMING THE SECONDARY STRUCTURE INTO A TIME SERIES

We can transform the secondary structure in the dot-bracket notation into a time series by “Single value mapping”, where “(” maps to 1, “.” maps to 0, and “)” maps to -1 .

C. TIME SERIES CLASSIFICATION

In univariate time series classification, an instance in the dataset consists of a time series $x = x_1, x_2, \dots, x_m$ with m observations and a discrete class label y , which takes c possible values [29], [30]. If $c = 2$, we refer to binary classification. If $c > 2$, we refer to multi-class classification. In multivariate time series classification, the time series is not a single sequence but a list of sequences. Each sequence is called a channel. There are many classifiers defined for time series data, including distance-based, feature-based, interval-based, shapelet-based, dictionary-based, convolution-based, and deep learning-based classifiers. Additionally, two or more of the above approaches can be combined, resulting in hybrid approaches [29], [30], [31]. We employed convolution-based classifiers due to their simplicity and accuracy.

1) CONVOLUTION-BASED CLASSIFIERS

Convolution-based classifiers first use randomly parameterized kernels to perform convolutions on the original time series T . A kernel is referred to as parameterized because its behavior is governed by a set of parameters, which will be discussed in detail later. Convolution is an operation to transform T to another time series M , where M is called the activation map. Its entry M_i is calculated by applying a kernel ω with length l to T at position i ,

TABLE 4. Time series encoding. P is the corresponding base-pair probability sequence of S . $p_i = 1$ if we encode S without incorporating base-pair probability sequence.

	Encoding	Algorithm	Example
1	Single value mapping [18], [20]–[23]	<p>for $i = 1$ to S:</p> $t_i = \begin{cases} 2 \cdot p_i & \text{if } s_i = A \\ 1 \cdot p_i & \text{if } s_i = G \\ -1 \cdot p_i & \text{if } s_i = C \\ -2 \cdot p_i & \text{if } s_i = U \\ 0 & \text{otherwise} \end{cases}$ <p>return T</p>	<p>Without base-pair probability sequence: $T = -1, 0, -1, -2, 1, -2, -2, 1, 2, -2$</p> <p>With base-pair probability sequence: $T = -0.843, 0.000, -0.807, -1.614, 0.793, -1.829, -1.963, 1.000, 1.999, -1.998$</p>
2	Grouped variable-length channel mapping	<p>$j = 1, k = 1$</p> <p>for $i = 1$ to S:</p> $t_j^1 = \begin{cases} 1 \cdot p_i & \text{if } s_i = A \\ -1 \cdot p_i & \text{if } s_i = U \\ 0 & \text{otherwise} \end{cases}$ $t_k^2 = \begin{cases} 1 \cdot p_i & \text{if } s_i = G \\ -1 \cdot p_i & \text{if } s_i = C \\ \text{if } (s_i = G) \text{ or } (s_i = C): \\ \quad \text{increment } k \text{ by 1} \\ \text{else:} \\ \quad \text{increment } j \text{ by 1} \end{cases}$ <p>return T^1, T^2</p>	<p>Without base-pair probability sequence: $T^1 = 0, -1, -1, -1, 1, -1$ $T^2 = -1, -1, 1, 1$</p> <p>With base-pair probability sequence: $T^1 = 0.000, -0.807, -0.914, -0.982, 0.999, -0.999$ $T^2 = -0.843, -0.807, 0.793, 1.000$</p>
3	Grouped fixed-length channel mapping	<p>for $i = 1$ to S:</p> $t_i^1 = \begin{cases} 1 \cdot p_i & \text{if } s_i = A \\ -1 \cdot p_i & \text{if } s_i = U \\ 0 & \text{otherwise} \end{cases}$ $t_i^2 = \begin{cases} 1 \cdot p_i & \text{if } s_i = G \\ -1 \cdot p_i & \text{if } s_i = C \\ 0 & \text{otherwise} \end{cases}$ <p>return T^1, T^2</p>	<p>Without base-pair probability sequence: $T^1 = 0, 0, -1, 0, -1, -1, 0, 1, -1$ $T^2 = -1, 0, -1, 0, 1, 0, 0, 1, 0, 0$</p> <p>With base-pair probability sequence: $T^1 = 0.000, 0.000, 0.000, -0.807, 0.000, -0.914, -0.982, 0.000, 0.999, -0.999$ $T^2 = -0.843, 0.000, -0.807, 0.000, 0.793, 0.000, 0.000, 1.000, 0.000, 0.000$</p>
4	Cumulative mapping [27], [28]	<p>$t_1 = 0$</p> <p>for $i = 1$ to S:</p> $t_{i+1} = \begin{cases} t_i + 2 \cdot p_i & \text{if } s_i = A \\ t_i + 1 \cdot p_i & \text{if } s_i = G \\ t_i - 1 \cdot p_i & \text{if } s_i = C \\ t_i - 2 \cdot p_i & \text{if } s_i = U \\ t_i & \text{otherwise} \end{cases}$ <p>return $T // T = S + 1$</p>	<p>Without base-pair probability sequence: $T = 0, -1, -1, -2, -4, -3, -5, -7, -6, -4, -6$</p> <p>With base-pair probability sequence: $T = 0.000, -0.843, -0.843, -1.650, -3.265, -2.471, -4.300, -6.263, -5.264, -3.265, -5.263$</p>
5	Cumulative grouped variable-length channel mapping	<p>$t_1^1 = 0, t_1^2 = 0$</p> <p>$j = 1, k = 1$</p> <p>for $i = 1$ to S:</p> $t_{j+1}^1 = \begin{cases} t_j^1 + 1 \cdot p_i & \text{if } s_i = A \\ t_j^1 - 1 \cdot p_i & \text{if } s_i = U \\ t_j^1 & \text{if } s_i = _ \end{cases}$ $t_{k+1}^2 = \begin{cases} t_k^2 + 1 \cdot p_i & \text{if } s_i = G \\ t_k^2 - 1 \cdot p_i & \text{if } s_i = C \\ \text{if } (s_i = G) \text{ or } (s_i = C): \\ \quad \text{increment } k \text{ by 1} \\ \text{else:} \\ \quad \text{increment } j \text{ by 1} \end{cases}$ <p>return T^1, T^2</p>	<p>Without base-pair probability sequence: $T^1 = 0, -1, -2, -3, -2, -3$ $T^2 = 0, -1, -2, -1, 0$</p> <p>With base-pair probability sequence: $T^1 = 0.000, -0.807, -1.722, -2.703, -1.704, -2.703$ $T^2 = 0.000, -0.843, -1.650, -0.857, 0.143$</p>
6	Cumulative grouped fixed-length channel mapping	<p>$t_1^1 = 0, t_1^2 = 0$</p> <p>for $i = 1$ to S:</p> $t_{i+1}^1 = \begin{cases} t_i^1 + 1 \cdot p_i & \text{if } s_i = A \\ t_i^1 - 1 \cdot p_i & \text{if } s_i = U \\ t_i^1 & \text{otherwise} \end{cases}$ $t_{i+1}^2 = \begin{cases} t_i^2 + 1 \cdot p_i & \text{if } s_i = G \\ t_i^2 - 1 \cdot p_i & \text{if } s_i = C \\ t_i^2 & \text{otherwise} \end{cases}$ <p>return $T^1, T^2 // T = T^2 = S + 1$</p>	<p>Without base-pair probability sequence: $T^1 = 0, 0, 0, -1, -2, -3, -3, -2, -3$ $T^2 = 0, -1, -1, -2, -2, -1, -1, 0, 0, 0$</p> <p>With base-pair probability sequence: $T^1 = 0.000, 0.000, 0.000, 0.000, -0.807, -0.807, -1.722, -2.703, -2.703, -1.704, -2.703$ $T^2 = 0.000, -0.843, -0.843, -1.650, -1.650, -0.857, -0.857, -0.857, -0.857, 0.143, 0.143, 0.143$</p>

396 defined as follows:

$$397 M_i = T(i : i + l - 1) * \omega = \sum_{j=0}^{l-1} t_{i+j} \cdot \omega_{1+j}$$

398 To note, $|T(i : i + l - 1)| = |\omega| = l$. Entries M_i 's
399 are calculated by sliding ω across T and computing a dot
400 product. Additionally, although the original paper [32] used

401 the term “convolution” to refer to the above operation,
402 “cross-correlation” may be a more suitable term for this
403 operation. Recall T with length m has $(m - l + 1)$ sliding
404 windows of length l , given that the increment is 1,¹⁰ which
405 defines the length of M .

¹⁰One step to the right per time.

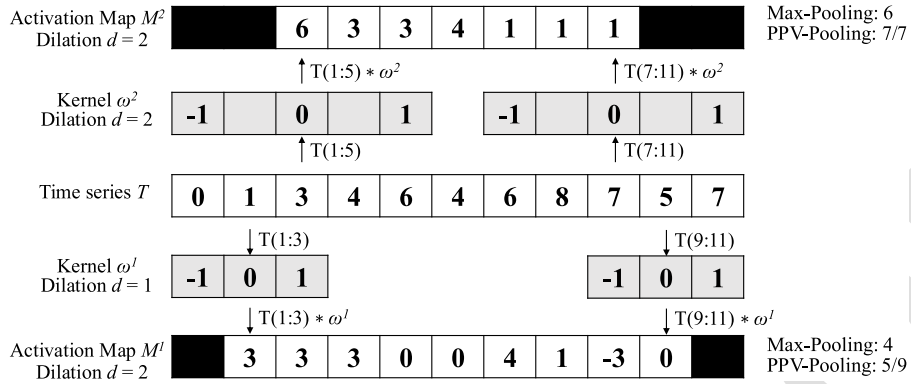


FIGURE 4. Features generation in the transformation.

Figure 4 shows two kernels ω^1 and ω^2 with lengths 3 and 5, respectively. Each of which performs a convolution with T and returns two activation maps, M^1 and M^2 , respectively. For example, $M_1^1 = T(1 : 3) * \omega^1 = 3$. By sliding ω^1 one time stamp at a time, an activation map M^1 with length = $(m - l + 1) = 11 - 3 + 1 = 9$ is obtained. Then, pooling operations, such as the maximum (MAX) and proportion of positive values (PPV), are applied on M^1 to derive the summary features. In Figure 4, MAX and PPV are applied on M^1 and M^2 . The summary features of M^1 are 4 and 5/9, which correspond to MAX and PPV, respectively. Dilation refers to a method that enables a kernel to cover a larger portion by creating empty spaces between entries in the kernel. The dilation d of ω^2 is 2. It introduces a gap of 1 in every two values of ω^2 .

The most popular convolution-based approach is the Random Convolutional Kernel Transform (ROCKET) [32]. It generates a large number of randomly parameterized kernels, ranging from thousands to tens of thousands. The kernel's parameters include length, weights (the entries inside the kernel), bias (the value added to the result of the convolution operation), and dilation. Additionally, padding can be applied to T at the start and end, ensuring M has the same length as the input. To note, T , M_1 , and M_2 in Figure 4 have different lengths. The summary statistics of the activation map are obtained through two pooling operations: MAX and PPV. Hence, for k kernels, the transformed data has $2k$ features. The default value of k is 10,000.

There are two extensions of ROCKET. They are MiniROCKET [33] and MultiROCKET [34]. MiniROCKET removes unnecessary operations and many of the random components in the definition of kernels used by ROCKET. It speeds up Rocket by over an order of magnitude with no significant difference in accuracy, making the classifier almost deterministic. For example, the kernel length is fixed, and only two weight values are used. Only PPV is used for the summary statistics. MultiROCKET is extended from MiniROCKET. The main improvement of it is to extract features from first-order differences as defined in Table 5

and add three new pooling operations [34]. The three added operations are mean of positive values (MPV), mean of indices of positive values (MIPV) and longest stretch of positive values (LSPV).

The HYbrid Dictionary-ROCKET Architecture (Hydra) combines dictionary-based and convolution-based models [35]. Similar to ROCKET-based classifiers, it uses random kernels to extract features from the input time series. But it groups the kernels into g groups of k kernels each, as shown in Figure 5. Each time series is passed through all the groups. For each group of kernels, we slide them across T and compute the dot product at each timestamp. Recall that the dot product of two input vectors (x and w_i) has the maximum value when the two vectors align in the same direction and the minimum value when they are oriented in opposite directions. We record the kernel that best matches the subsequence of T at each timestamp in each group (i.e., argmax). We refer to these kernels as the winning kernels. This results in a k -dimensional count vector for each of the g groups, where $k = 3$ in Figure 5. This results in a total of $g \times k$ features, with default values of $g = 64$ and $k = 8$. It uses a total of $k \times g = 512$ kernels per dilation. In addition to recording the kernel with the maximum response, we can also record the kernel with the minimum response, knowing that this kernel will be the best match with the “inverted” subsequence of T . Hydra is applied to both the original time series and its first-order differences. Hydra generated approximately 1000 features for each instance in our dataset. [35] found that it can improve the accuracy by concatenating features generated from Hydra with those from MultiRocket. This classifier is called MultiROCKET-Hydra.

These five classifiers share the same simple design pattern. It involves the overproduction of features followed by a selection strategy. A large number of features (1,000 ~ 50,000) are generated for each instance. The features are then fed into a simple linear classifier. It determines which features are most useful and returns the final classification result. A ridge classifier is used in this study. It is a linear classifier that extends ridge regression to classification tasks by applying a threshold to the predicted values.

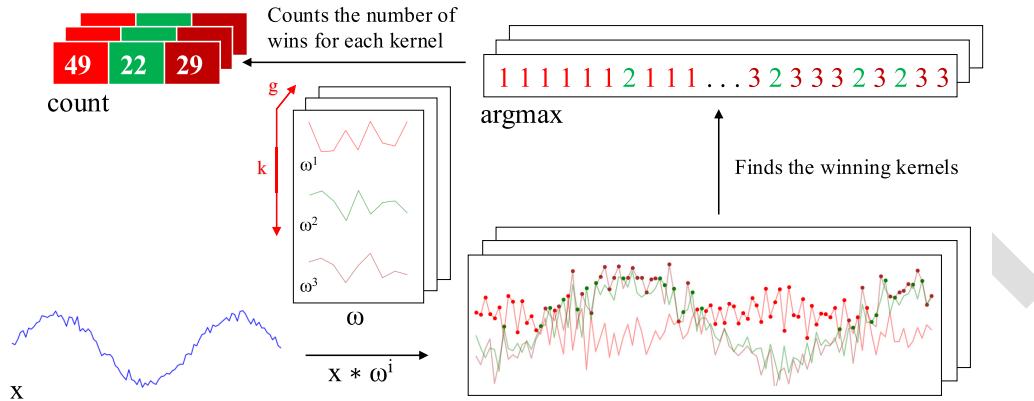


FIGURE 5. Convolutions of HYDRA for each input time series with a set of random kernels w , organized into g groups with k kernels each.

486 It uses L2 regularization to prevent overfitting. The regularization strength is selected by internal cross-validation.
 487 A Ridge classifier is suggested for small datasets, as in our
 488 case, while a logistic regression classifier is suggested for
 489 large datasets [31].

490 While these five classifiers are often referred to as classifiers [31], they are technically time series transformation methods for generating features that are then fed to a downstream classifier. The comparison of them is shown in Table 5. For MiniROCKET and MultiROCKET, the bias is determined from the convolution output, and the dilation depends on the length of the input time series [33], [34]. The main differences among ROCKET-based classifiers lie in how the summary features are generated. The generation of the summary features depends on:

- 501 1) Kernels, which are defined based on the parameters,
 502 which consist of kernel length, kernel weights, bias,
 503 and dilation.
- 504 2) The way that padding applies to T , which leads to
 505 activation maps with different lengths.
- 506 3) The pooling operations, which are used in extracting
 507 features on the activation map.

508 D. EVALUATION METRICS

509 To evaluate the performance of our time series-based classification (MTSC) model, we adopted five standard classification metrics. They are Accuracy (Acc), Specificity (Sp), Sensitivity (Sn), F1 score (F1), and Matthews Correlation Coefficient (MCC) [36].

$$\begin{aligned} 514 \quad Acc &= \frac{TP + TN}{TP + TN + FP + FN} \\ 515 \quad Sp &= \frac{TN}{TN + FP} \\ 516 \quad Sn &= \frac{TP}{TP + FN} \\ 517 \quad F1 &= \frac{2 \times TP}{2 \times TP + FP + FN} \end{aligned}$$

$$518 \quad MCC = \frac{TP \times TN - FP \times FN}{\sqrt{(TP + FP)(TP + FN)(TN + FP)(TN + FN)}}$$

519 where TP, TN, FP, and FN are the number of true
 520 positives, true negatives, false positives, and false negatives,
 521 respectively.

522 To extend a binary metric to multi-class problems, we can
 523 treat the data as a collection of binary problems, one for each
 524 class. One class is treated as positive while the other classes
 525 are treated as negative. Then, the multi-class metrics can be
 526 obtained by averaging binary metric calculations across the
 527 set of classes. There are different ways of doing the averaging.
 528 Here, we adopted a macro-averaging approach. It treats each
 529 class equally and calculates the mean of the binary metrics.
 530 To use MCC in the multiclass case, it can be defined in
 531 terms of a confusion matrix C for K classes, where $C_{i,j}$ is
 532 the number of observations that are actually in class i and
 533 predicted to be in class j [37].

$$534 \quad MCC_{multi} = \frac{c \times s - \sum_k^K p_k \times t_k}{\sqrt{(s^2 - \sum_k^K p_k^2) \times (s^2 - \sum_k^K t_k^2)}}$$

535 where $t_k = \sum_i^K C_{i,k}$ (denoting the number of times class k
 536 actually occurred), $p_k = \sum_i^K C_{k,i}$ (denoting the number of
 537 times class k was predicted), $c = \sum_k^K C_{k,k}$ (denoting the total
 538 number of samples correctly predicted) and $s = \sum_i^K \sum_j^K C_{i,j}$
 539 (denoting the total number of samples).

III. RESULTS

540 The code implementing our method is available at <https://github.com/colemanyu/time-series-classification-cleavage>. The
 541 dataset of this study is available at <https://www.mirbase.org>.

542 In all experiments, the models were trained and tested
 543 using 5-fold cross-validation. We retrieved 827 empirically
 544 validated sequences of pre-miRNAs. There are 5p arm and 3p
 545 arm in each sequence. For each arm, we defined a cleavage
 546 pattern and a non-cleavage pattern. Three datasets, namely
 547 “5p arm”, “3p arm”, and “multi-class” were constructed
 548 by these patterns. We refer to the cleavage patterns as positive
 549

TABLE 5. Comparison of rocket-based classifiers [31]. $\mathcal{N}(0, 1)$: a standard normal distribution, $U(0, 1)$: a uniform distribution between 0 and 1, 1st order difference: $\Delta T = t_2 - t_1, t_3 - t_2, \dots, t_n - t_{n-1}$.

	ROCKET	MiniROCKET	MultiROCKET	Hydra
kernel length	{7, 9, 11}	9	9	9
kernel weights	$\mathcal{N}(0, 1)$	{-1, 2}	{-1, 2}	$\mathcal{N}(0, 1)$
bias	$\mathcal{U}(0, 1)$	from output	from output	none
dilation	random	fixed (input-relative)	fixed (input-relative)	random
padding	random	fixed	fixed	always
pooling operations	MAX, PPV	PPV	PPV, MPV, MIPV, LSPV	Response per Kernel/Group
1 st order difference	no	no	yes	yes
feature vector size	20k	10k	50k	relative to input

551 instances and the non-cleavage patterns as negative instances.
 552 The 5p arm dataset comprises 827 positive instances and
 553 an equal number of negative instances. The 5p arm and 3p
 554 arm datasets are binary-class datasets. The multi-class dataset
 555 comprises all patterns from both the 5p arm and the 3p
 556 arm. There are 827 “5p” instances,¹¹ 827 “3p” instances,
 557 and 1,654 negative instances.

558 For every fold in 5-fold cross-validation, the dataset was
 559 divided into a training set and a test set with sizes of 80%
 560 and 20% of the whole dataset, respectively. We kept the class
 561 distribution approximately the same in each fold, since it is
 562 in the original dataset. In each fold derived from the 5p arm
 563 and 3p arm datasets, the training set has a size of 1,323, and
 564 the test set has a size of 331. In each fold derived from the
 565 multi-class dataset, the training set has a size of 2,262, and
 566 the test set has a size of 662. We reported the average of the
 567 five classification metrics.

568 The ROCKET-based classifiers require all channels
 569 in the multivariate time series to have equal length.
 570 We applied padding to the shorter channels with the constant
 571 value 100, which does not appear in the original time
 572 series. It ensures the padding does not introduce ambiguity
 573 or interfere with the semantic meaning of the encoded
 574 nucleotide signals.

A. CHANNEL IMPORTANCE STUDY

575 We utilized three types of data as the input features for
 576 each instance. They are (1) the RNA sequence, which
 577 consists of the primary strand and its complementary strand,
 578 (2) the secondary structure information, and (3) the base-
 579 pair probability sequence. To input the data into our time
 580 series-based classifiers, we converted them into multivariate
 581 time series. The primary strand and its complementary
 582 strand are each encoded into one or two channels, using
 583 the encoding methods in Table 4. For example, single value
 584 mapping encodes a strand in one channel, while grouped
 585 variable-length channel mapping encodes in two channels.
 586 The secondary structure information is converted into a
 587 univariate time series. The base-pair probability sequence is
 588 already in numerical form and does not require further trans-
 589 formation. It can be used either as a standalone channel or
 590 incorporated into the encoding of the complementary strand.

¹¹Cleavage patterns from the 5p arm.

We performed a channel importance study to determine the
 593 most informative combination of the above channels.

We referred to the multivariate time series that consists of
 594 the channels from the RNA sequence only as the baseline
 595 setting. We added the other channels to this baseline. It leads
 596 to the following configurations (cfgs):

- 1) (cfg 1) Baseline: Time series derived only from the
 598 RNA sequence.
- 2) (cfg 2) Baseline + Secondary structure: Baseline +
 600 time series representation of the secondary structure.
- 3) (cfg 3) Baseline + Base-pair probability (Standalone):
 602 Baseline + the base-pair probability sequence as a
 603 standalone channel.
- 4) (cfg 4) Baseline + Base-Pair probability (Incorpo-
 605 rated): Baseline with the base-pair probability sequence
 606 incorporated into the encoding of the complementary
 607 strand.

We used single value mapping as the encoding method.
 609 Table 6 shows the result. From the table, we can see that
 610 the addition of secondary structure, base-pair probability as
 611 a standalone channel, and base-pair probability incorporated
 612 in the encoding of the complementary strand can improve
 613 the performance. We plotted the critical difference (CD)
 614 diagram as shown in Figure 6 to visualize Table 6 to make
 615 the performances of different combinations more obvious.
 616 In CD diagrams, lower-ranked methods (toward the right) are
 617 better. A horizontal bar connecting combinations indicates no
 618 statistically significant difference.

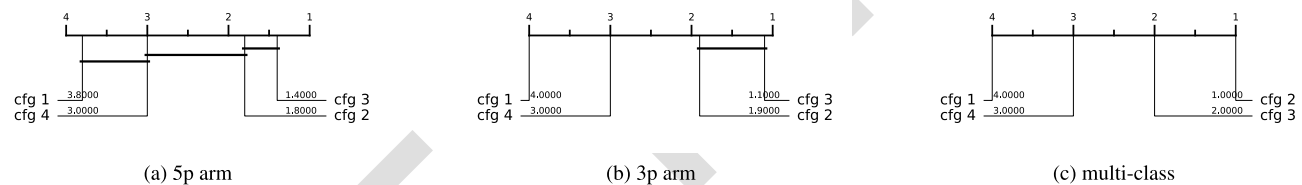
619 From Figure 6, we can see that including time series
 620 derived from secondary structure information and base-pair
 621 probability as a separate channel can significantly improve
 622 the performance of the classifiers. Incorporating the base-
 623 pair probability sequence in the time series encoding of the
 624 complementary strand can also improve the classifier, but to
 625 a minor degree compared to serving as a standalone channel.
 626 In our downstream analysis, we adopted the combination
 627 of RNA sequence time series (2 to 4 channels), secondary
 628 structure time series (1 channel), and base-pair probability
 629 time series (1 channel) as our multivariate time series input,
 630 with 4 to 6 channels, depending on the encoding used.

B. PREDICTIVE PERFORMANCE

632 The experiment was conducted on three datasets: the 5p arm,
 633 the 3p arm, and the multi-class datasets. Recall that we have

TABLE 6. Channel importance study. The best results are highlighted in bold.

Classifier	5p arm					3p arm					multi-class					
	Acc	Sp	Sn	F1	MCC	Acc	Sp	Sn	F1	MCC	Acc	Sp	Sn	F1	MCC	
Baseline (cfg 1)	ROCKET	0.781	0.743	0.819	0.789	0.563	0.790	0.773	0.807	0.793	0.580	0.717	0.838	0.685	0.700	0.538
	MiniROCKET	0.755	0.728	0.782	0.762	0.512	0.788	0.781	0.794	0.789	0.576	0.685	0.823	0.653	0.662	0.486
	MultiROCKET	0.784	0.767	0.801	0.787	0.569	0.803	0.792	0.814	0.805	0.606	0.691	0.830	0.667	0.672	0.501
	Hydra	0.830	0.800	0.860	0.835	0.663	0.808	0.797	0.820	0.810	0.617	0.731	0.844	0.696	0.712	0.560
	MultiROCKET-Hydra	0.796	0.778	0.815	0.800	0.594	0.807	0.767	0.816	0.808	0.614	0.701	0.836	0.681	0.686	0.520
Baseline + Secondary Structure (cfg 2)	ROCKET	0.847	0.832	0.862	0.849	0.695	0.855	0.842	0.868	0.857	0.711	0.836	0.907	0.828	0.833	0.736
	MiniROCKET	0.825	0.807	0.843	0.827	0.652	0.822	0.802	0.843	0.826	0.646	0.823	0.900	0.812	0.818	0.715
	MultiROCKET	0.812	0.803	0.822	0.814	0.626	0.824	0.809	0.839	0.826	0.649	0.796	0.888	0.791	0.792	0.673
	Hydra	0.845	0.816	0.873	0.849	0.691	0.846	0.817	0.874	0.850	0.693	0.830	0.901	0.814	0.826	0.724
	MultiROCKET-Hydra	0.817	0.809	0.826	0.819	0.635	0.825	0.816	0.834	0.826	0.652	0.803	0.891	0.798	0.800	0.684
Baseline + Base-pair probability (Standalone) (cfg 3)	ROCKET	0.842	0.828	0.855	0.844	0.684	0.855	0.856	0.854	0.855	0.710	0.795	0.885	0.783	0.789	0.670
	MiniROCKET	0.817	0.820	0.814	0.816	0.634	0.836	0.834	0.838	0.836	0.673	0.772	0.872	0.757	0.764	0.632
	MultiROCKET	0.822	0.813	0.832	0.824	0.645	0.825	0.831	0.820	0.824	0.651	0.758	0.866	0.747	0.750	0.612
	Hydra	0.846	0.827	0.865	0.849	0.693	0.851	0.840	0.861	0.852	0.702	0.789	0.879	0.769	0.780	0.658
	MultiROCKET-Hydra	0.822	0.809	0.834	0.824	0.644	0.835	0.840	0.830	0.834	0.670	0.759	0.866	0.746	0.750	0.611
Baseline + Base-pair probability (Incorporated) (cfg 4)	ROCKET	0.799	0.771	0.827	0.805	0.600	0.809	0.786	0.832	0.813	0.619	0.737	0.850	0.712	0.724	0.573
	MiniROCKET	0.776	0.756	0.797	0.781	0.554	0.801	0.808	0.794	0.799	0.603	0.705	0.835	0.675	0.684	0.521
	MultiROCKET	0.814	0.801	0.828	0.817	0.630	0.816	0.812	0.820	0.816	0.634	0.726	0.848	0.706	0.712	0.556
	Hydra	0.822	0.787	0.857	0.828	0.647	0.834	0.828	0.840	0.835	0.669	0.759	0.862	0.734	0.746	0.608
	MultiROCKET-Hydra	0.814	0.802	0.820	0.817	0.629	0.820	0.825	0.816	0.819	0.642	0.736	0.853	0.717	0.723	0.874

**FIGURE 6.** CD diagrams of channel importance study.

nine encoding methods and five ROCKET-based classifiers. It results in 45 combinations of encoding methods and classifiers.

The result is shown in Table 7. The best combination of encoding method and classifier is shown in Table 8. For the 5p arm dataset, the best combination is “Global Cumulative grouped fixed-length channel mapping + ROCKET”. For all five classification metrics, it outperforms the state-of-the-art (SOTA) method, DiCleave. For the 3p arm dataset, the best combination is “Global Cumulative grouped fixed-length channel mapping + ROCKET”. Out of the five classification metrics, it outperforms DiCleave, except in specificity. For the multi-class dataset, the best combination is “Global Cumulative grouped fixed-length channel mapping + ROCKET”. For all five classification metrics, it outperforms DiCleave. Note that for the 3p arm and the multi-class datasets, the combination of “Cumulative grouped fixed-length channel mapping + ROKCET” also attains the best result.

To summarize Table 7, we plot the CD diagrams for finding the best classifier, which is ROCKET in all cases, as shown in Figure 7, and the best encoding method, which is enc 9 in the 5p arm dataset and enc 7 for the others, as shown in Figure 8. It is suggested to use ROCKET as the baseline classifier. For the encoding, it is suggested to use enc 7 or enc 9.

C. RUNNING TIME ANALYSIS

To compare the computational efficiency of MTSCCleav and DiCleave, we conducted a comparative analysis of their running times. For DiCleave, we employed the code from its supporting website,¹² without any modifications. All experiments were conducted on the same machine (a personal laptop equipped with an Apple M1 Pro chip and 16 GB of memory) and using the same splits of the training and test datasets under 5-fold cross-validation to ensure fairness. The reported running times are the averages of the five runs. The timing results were measured from the training phase to the return of the five classification metrics. The result is shown in Table 8. MiniROCKET is the most computationally efficient of the five rocket-based classifiers. We also included its best result, along with the corresponding encoding method, even though this combination may not be the best overall.

MTSCCleav demonstrated a significant advantage in computational efficiency, achieving an average 27.0X, 3.7X, and 10.7X speedup over DiCleave, for the 5p arm, 3p arm, and multi-class datasets, respectively. If we consider using the MiniROCKET in the case of 3p arm and multi-class datasets, it achieves 16.1X and 28.8X speedup. To note, in the case of the 3p arm dataset, the performance of MiniROCKET

¹²<https://github.com/MGuard0303/DiCleave> (Accessed on: 2025-07-13).

TABLE 7. Performance on the 45 combinations between encoding methods and the ROCKET-based classifiers. The best results are highlighted in bold.

Classifier	5p arm					3p arm					multi-class					
	Acc	Sp	Sn	F1	MCC	Acc	Sp	Sn	F1	MCC	Acc	Sp	Sn	F1	MCC	
Single value mapping (enc 1)	ROCKET	0.849	0.842	0.857	0.851	0.699	0.863	0.854	0.873	0.865	0.727	0.853	0.917	0.847	0.851	0.764
	MiniROCKET	0.823	0.809	0.837	0.825	0.647	0.823	0.828	0.817	0.822	0.647	0.835	0.906	0.828	0.833	0.735
	MultiROCKET	0.821	0.802	0.840	0.824	0.643	0.839	0.826	0.852	0.841	0.679	0.811	0.894	0.806	0.809	0.697
	Hydra	0.843	0.820	0.867	0.847	0.688	0.838	0.819	0.857	0.841	0.677	0.831	0.901	0.815	0.827	0.727
	MultiROCKET-Hydra	0.820	0.803	0.837	0.823	0.640	0.840	0.830	0.850	0.841	0.680	0.816	0.896	0.810	0.814	0.704
Grouped variable-length channel mapping (enc 2)	ROCKET	0.835	0.826	0.844	0.836	0.670	0.855	0.849	0.861	0.856	0.710	0.846	0.913	0.839	0.844	0.752
	MiniROCKET	0.843	0.833	0.853	0.844	0.686	0.831	0.821	0.842	0.833	0.663	0.837	0.907	0.828	0.834	0.737
	MultiROCKET	0.819	0.809	0.828	0.820	0.638	0.817	0.814	0.820	0.818	0.634	0.890	0.894	0.806	0.808	0.695
	Hydra	0.825	0.780	0.869	0.832	0.653	0.811	0.769	0.854	0.819	0.626	0.818	0.892	0.765	0.812	0.705
	MultiROCKET-Hydra	0.818	0.814	0.822	0.819	0.636	0.831	0.825	0.837	0.832	0.662	0.820	0.900	0.815	0.818	0.710
Grouped fixed-length channel mapping (enc 3)	ROCKET	0.851	0.843	0.859	0.852	0.702	0.863	0.850	0.875	0.864	0.726	0.849	0.915	0.843	0.847	0.757
	MiniROCKET	0.844	0.836	0.853	0.845	0.689	0.840	0.826	0.855	0.843	0.682	0.851	0.915	0.844	0.849	0.760
	MultiROCKET	0.831	0.815	0.848	0.834	0.663	0.824	0.813	0.836	0.826	0.649	0.811	0.896	0.808	0.808	0.698
	Hydra	0.848	0.816	0.880	0.853	0.699	0.862	0.839	0.884	0.864	0.724	0.843	0.908	0.837	0.839	0.746
	MultiROCKET-Hydra	0.836	0.813	0.859	0.839	0.672	0.833	0.820	0.845	0.835	0.665	0.828	0.905	0.824	0.826	0.725
Cumulative mapping (enc 4)	ROCKET	0.850	0.834	0.866	0.852	0.701	0.863	0.855	0.871	0.864	0.726	0.852	0.915	0.842	0.850	0.762
	MiniROCKET	0.840	0.821	0.860	0.843	0.682	0.840	0.837	0.844	0.841	0.682	0.843	0.911	0.835	0.840	0.747
	MultiROCKET	0.822	0.809	0.834	0.824	0.644	0.832	0.830	0.834	0.832	0.665	0.820	0.898	0.810	0.816	0.709
	Hydra	0.848	0.819	0.878	0.853	0.698	0.853	0.856	0.869	0.855	0.705	0.845	0.910	0.830	0.841	0.749
	MultiROCKET-Hydra	0.824	0.811	0.856	0.825	0.647	0.838	0.833	0.843	0.839	0.677	0.821	0.898	0.810	0.817	0.711
Cumulative grouped variable-length channel mapping (enc 5)	ROCKET	0.843	0.821	0.866	0.847	0.688	0.856	0.840	0.871	0.857	0.712	0.855	0.916	0.843	0.851	0.766
	MiniROCKET	0.845	0.826	0.865	0.848	0.691	0.836	0.833	0.838	0.836	0.672	0.840	0.909	0.833	0.838	0.742
	MultiROCKET	0.826	0.814	0.838	0.828	0.653	0.815	0.820	0.810	0.814	0.631	0.826	0.902	0.820	0.824	0.721
	Hydra	0.850	0.819	0.880	0.854	0.701	0.834	0.807	0.861	0.838	0.669	0.833	0.903	0.818	0.829	0.731
	MultiROCKET-Hydra	0.824	0.810	0.838	0.826	0.649	0.833	0.833	0.833	0.833	0.666	0.830	0.903	0.821	0.827	0.726
Cumulative grouped fixed-length channel mapping (enc 6)	ROCKET	0.856	0.836	0.876	0.858	0.712	0.870	0.861	0.879	0.871	0.741	0.863	0.921	0.852	0.860	0.780
	MiniROCKET	0.856	0.837	0.874	0.858	0.712	0.842	0.839	0.845	0.843	0.685	0.845	0.912	0.837	0.843	0.751
	MultiROCKET	0.820	0.802	0.839	0.824	0.642	0.798	0.798	0.798	0.798	0.597	0.809	0.894	0.806	0.807	0.694
	Hydra	0.850	0.814	0.885	0.855	0.701	0.855	0.840	0.869	0.857	0.711	0.847	0.910	0.831	0.843	0.752
	MultiROCKET-Hydra	0.820	0.801	0.839	0.823	0.641	0.807	0.813	0.802	0.806	0.615	0.821	0.900	0.817	0.819	0.713
Global Cumulative mapping (enc 7)	ROCKET	0.850	0.834	0.866	0.852	0.701	0.863	0.855	0.871	0.864	0.726	0.852	0.915	0.842	0.850	0.762
	MiniROCKET	0.847	0.832	0.862	0.849	0.695	0.848	0.839	0.857	0.850	0.697	0.845	0.911	0.836	0.843	0.750
	MultiROCKET	0.827	0.819	0.834	0.828	0.653	0.847	0.842	0.853	0.848	0.695	0.825	0.901	0.817	0.822	0.718
	Hydra	0.851	0.821	0.880	0.855	0.703	0.861	0.848	0.874	0.863	0.722	0.847	0.911	0.834	0.844	0.753
	MultiROCKET-Hydra	0.829	0.823	0.834	0.830	0.658	0.843	0.838	0.849	0.844	0.688	0.832	0.905	0.823	0.829	0.730
Global Cumulative grouped variable-length channel mapping (enc 8)	ROCKET	0.840	0.814	0.867	0.844	0.682	0.853	0.838	0.867	0.854	0.706	0.856	0.917	0.845	0.853	0.768
	MiniROCKET	0.848	0.834	0.862	0.850	0.697	0.841	0.824	0.859	0.844	0.683	0.844	0.911	0.856	0.842	0.748
	MultiROCKET	0.834	0.828	0.839	0.834	0.668	0.831	0.821	0.842	0.833	0.663	0.828	0.904	0.823	0.826	0.724
	Hydra	0.857	0.821	0.894	0.862	0.717	0.822	0.786	0.857	0.828	0.645	0.826	0.898	0.806	0.820	0.717
	MultiROCKET-Hydra	0.837	0.834	0.839	0.837	0.674	0.834	0.827	0.840	0.835	0.668	0.835	0.907	0.828	0.832	0.734
Global Cumulative grouped fixed-length channel mapping (enc 9)	ROCKET	0.856	0.836	0.876	0.858	0.712	0.870	0.861	0.879	0.871	0.741	0.863	0.921	0.852	0.860	0.780
	MiniROCKET	0.857	0.845	0.870	0.859	0.715	0.840	0.821	0.859	0.843	0.681	0.844	0.911	0.837	0.842	0.749
	MultiROCKET	0.829	0.825	0.833	0.830	0.658	0.820	0.816	0.823	0.820	0.640	0.819	0.900	0.816	0.817	0.710
	Hydra	0.856	0.817	0.894	0.861	0.713	0.859	0.838	0.880	0.862	0.719	0.846	0.911	0.832	0.843	0.752
	MultiROCKET-Hydra	0.829	0.824	0.834	0.830	0.658	0.822	0.825	0.819	0.821	0.644	0.827	0.904	0.823	0.824	0.722

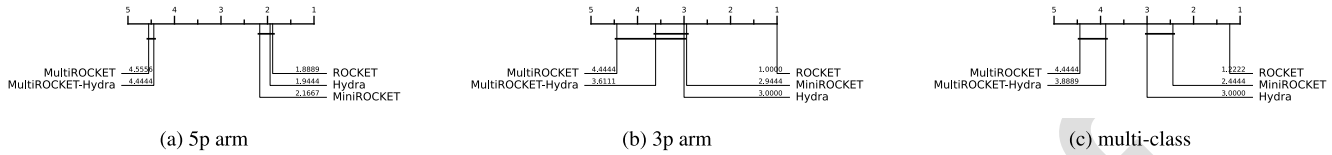
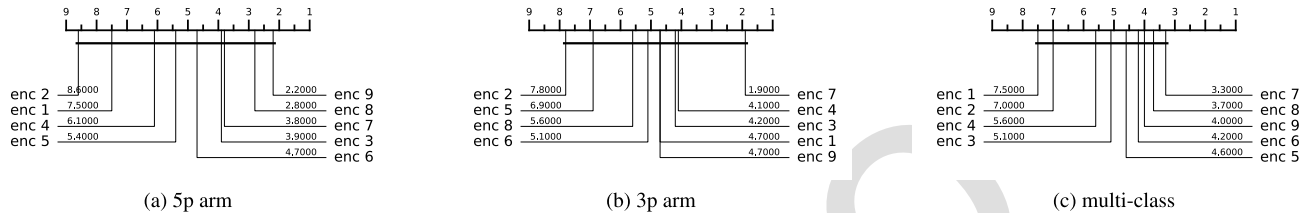
TABLE 8. Comparative analysis between MTSCClean with the best combination of the encoding method and classifier, with the SOTA, DiCleave, on the three datasets. The best results of using MiniROCKET have also been shown to compare the computational efficiency. The best results are highlighted in bold.

Dataset	Methods	Acc	Sp	Sn	F1	MCC	Time (s)
5p arm	enc 9 + MiniROCKET	0.857	0.845	0.870	0.859	0.715	0.787
	DiCleave	0.818	0.790	0.846	0.822	0.653	21.249
	enc 7 + ROCKET	0.870	0.861	0.879	0.871	0.741	4.311
3p arm	enc 9 + MiniROCKET	0.848	0.839	0.857	0.850	0.697	0.989
	DiCleave	0.854	0.891	0.817	0.847	0.715	15.919
	enc 9 + ROCKET	0.863	0.921	0.852	0.860	0.780	12.208
multi-class	enc 3 + MiniROCKET	0.851	0.915	0.844	0.849	0.760	4.550
	DiCleave	0.820	0.895	0.804	0.815	0.710	131.151

is only slightly worse than DiCleave. In the case of the multi-class dataset, even the performance of MiniROCKET is better than DiCleave. DiCleave is a deep learning-based method that requires substantial time for model inference, while MTSCClean leverages efficient ROCKET-based classifiers. This significant reduction in runtime makes MTSCClean more suitable for large-scale data and real-time applications.

D. SUBSEQUENCE IMPORTANCE

To evaluate the sensitivity of MTSCClean to subsequences of the input, we conducted a perturbation experiment to evaluate the importance of subsequences based on masking windows. The goal of this experiment is to identify which subsequences of the entire time series are critical for classification. We examine how various modifications to the

**FIGURE 7.** CD diagrams to compare different classifiers.**FIGURE 8.** CD diagrams to compare different encoding methods.

original input impact model performance. It suggests which features are essential for classification.

The model was trained on the original training dataset. For each instance in the test dataset, we measure its original score and the masked score. We slid a masking window w with a fixed length over the input time series T . $|w|$ was set to 4, which is about one third of the whole length. For each window position $i \in \{1, 2, \dots, |T| - |w| + 1\}$, we masked all entries across all the channels of T within the window. Hence, we removed or hid that portion of information from the model during inference. The changes in classification performance in terms of accuracy relative to the unmasked original score of each i are recorded. Intuitively, if the information of a subsequence is critical for the classification, the masking of this subsequence would lead to a great drop in classification performance. We aggregated the importance score across the test dataset.

The result is shown in Figure 9. For the encoding methods, we cannot use the methods derived from the cumulative mapping because the accumulation would leak information from the masked region. We adopted “Grouped fixed-length channel mapping” as the encoding method and ROCKET as the classifier. “Grouped fixed-length channel mapping” is the best encoding, other than the methods derived from the cumulative mapping, in all datasets, as shown in Figure 8. ROCKET is the best classifier, as shown in Figure 7.

In the 5p arm dataset, we found that masking subsequences at the tailing part caused a significant drop in the importance score, as shown in Figure 9 (a). In the 3p arm dataset, we found that masking subsequences at the leading part caused a significant drop in the importance score, as shown in Figure 9 (b).

E. SUMMARY

Our method achieves better or comparable predictive results and a 3.7X to 28.8X speedup compared to the state-of-the-art (SOTA).

IV. DISCUSSION

The channel importance study reveals that the involvement of the time series derived from the secondary structure can improve accuracy. It suggests the importance of RNA folding in Dicer processing. Furthermore, we found that the base-pair probability sequence of the secondary structure can also enhance accuracy. To the best of our knowledge, it is a novel application of the base-pair probability sequence. Experiments show that using the probability sequence as an additional channel can enhance accuracy more than incorporating it in the encoding. It is likely because keeping it as an additional channel can preserve more information, of both the probability sequence itself and the complementary strand.

Out of the three datasets, the best classifier is ROCKET. The ranking of the five classifiers by performance, starting from the best, is as follows: ROCKET, MiniROCKET, Hydra, MultiROCKET-Hydra, and MultiROCKET, where the ranking of Hydra and MiniROCKET is interchanged in different cases. It indicates that the features created from the pooling operations that are only in MultiROCKET but not in MiniROCKET, confuse the final classifier. They are mean of positive values (MPV), mean of indices of positive values (MIPV) and longest stretch of positive values (LSPV) [34]. In contrast, the pooling operator that is only present in ROCKET but not in MiniROCKET, enhances the classification performance. It is maximum (MAX).

For the encoding methods, we have the following observations. Fixed-length grouped channel mappings outperform variable-length counterparts with one exception in the multi-class dataset, likely because fixed-length schemes better preserve the original positional information of nucleotides within the sequence. Global cumulative methods consistently yield better performance than local cumulative methods. It suggests that the upstream information of the cleavage pattern plays a critical role in identifying cleavage sites. Cumulative-based encodings perform better than single-value mappings, with one exception in the 3p dataset,

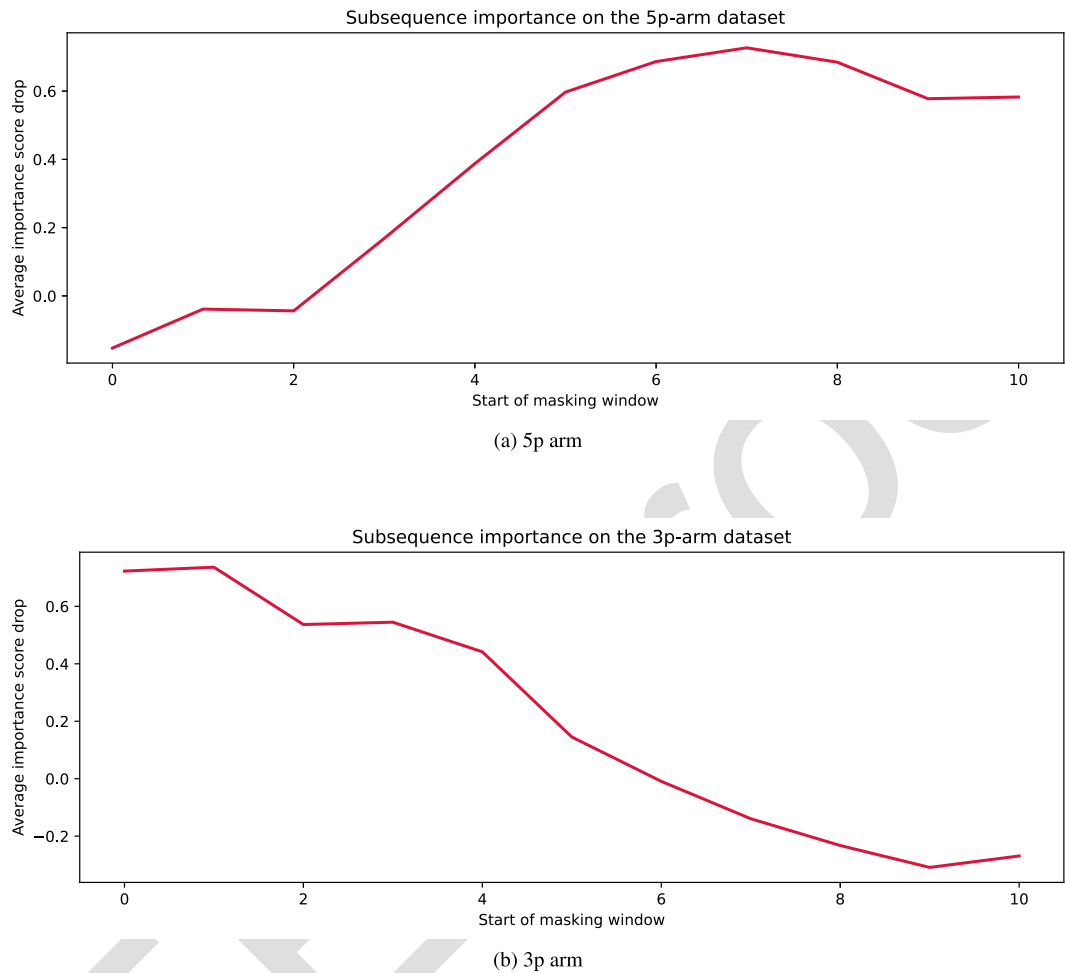


FIGURE 9. Results of the perturbation experiment.

774 suggesting that the accumulated nucleotide signal is more
 775 informative for cleavage site prediction than the local or
 776 isolated presence of nucleotides. According to Figure 8 (b),
 777 for the 3p arm dataset, encoding RNA sequence in two
 778 channels in a global cumulative manner (i.e., enc 9) appears to
 779 worsen the result. This suggests that the 5p arm and 3p arm
 780 datasets may require different nucleotide grouping methods
 781 for encoding.

782 One limitation of DiCleave is overfitting during training
 783 because of the relatively small size of the dataset [11].
 784 DiCleave is a deep learning-based method. Deep learning
 785 models typically require a large amount of training data
 786 to generalize effectively. They are data-hungry. In contrast,
 787 MTSCcleav leverages ROCKET-based methods for the
 788 classification. They rely on random convolutional feature
 789 extraction followed by a simple linear classifier. The Ridge
 790 classifier used in this study is less data-hungry compared to
 791 deep learning methods due to its use of L2 regularization and
 792 the simplicity of its linear model nature. It allows ROCKET-
 793 based classifiers, and hence MTSCcleav, to maintain strong
 794 predictive performance even in settings with a relatively small
 795 dataset size.

796 The subsequence importance reveals some connections
 797 between RNA secondary structure and human Dicer cleavage
 798 site prediction. The perturbation experiment shows that the
 799 leading part of 5p arm and the tailing part of 3p arm are
 800 important for the classification. These parts are close to
 801 the center of the RNA secondary structure of pre-miRNA.
 802 It indicates that the center region is more crucial for human
 803 Dicer cleavage site prediction. It is consistent with the
 804 previous study [10].

V. CONCLUSION

805 We proposed an accurate, fast, and simple multivariate
 806 time series classification (MTSC)-based method, termed
 807 MTSCcleav, for predicting human Dicer cleavage sites.
 808 Base-pair probability sequences of the secondary structures
 809 have also been leveraged in the classification. MTSCcleav
 810 consists of three parts: time series encoding, time series
 811 transformation, and classification. ROCKET-based methods
 812 were used for time series transformation. Ridge Classifier
 813 was used for classification. For the computational experi-
 814 ments, we evaluated nine time series encoding methods in
 815 conjunction with five time series transformation methods.

817 MTSCCleav outperformed the SOTA method in all five
 818 evaluation metrics for the 5p-arm and multi-class datasets,
 819 and four of the metrics for the 3p-arm dataset. In terms
 820 of computational efficiency, MTSCCleav with the optimal
 821 setting achieved an average 3.7X to 27.0X speedup over
 822 the SOTA method on the three datasets. With the use of
 823 a less accurate but faster time series classification method,
 824 MTSCCleav achieved an average speedup of 16.1X to 28.8X,
 825 respectively. We analyzed the subsequence importance of
 826 the input multivariate time series. The results show that
 827 subsequences near the center of the pre-miRNA sequences
 828 are more important. This aligns with the findings from
 829 previous work. This study demonstrates that time series
 830 analysis provides a powerful alternative to conventional
 831 modeling in the context of RNA processing. This framework
 832 may be extended to other RNA-processing tasks. Notably,
 833 the encoding of RNA sequence into time series enables us
 834 to utilize any well-established tools from the time series
 835 community.

REFERENCES

- [1] L. A. Urry, M. L. Cain, S. A. Wasserman, P. V. Minorsky, R. B. Orr, and N. A. Campbell, *Campbell Biology*, 12th ed., New York, NY, USA: Pearson, 2020.
- [2] B. Alberts, *Molecular Biology of the Cell*, 7th ed., New York, NY, USA: Norton & Company, 2022.
- [3] W. W. Cohen, *A Computer Scientist's Guide to Cell Biology: A Travelogue From a Stranger in a Strange Land*. New York, NY, USA: Springer, 2007.
- [4] Y. Lee, “MicroRNA maturation: Stepwise processing and subcellular localization,” *EMBO J.*, vol. 21, no. 17, pp. 4663–4670, Sep. 2002.
- [5] S. Gu, L. Jin, Y. Zhang, Y. Huang, F. Zhang, P. N. Valdmanis, and M. A. Kay, “The loop position of shRNAs and pre-miRNAs is critical for the accuracy of Dicer processing in vivo,” *Cell*, vol. 151, no. 4, pp. 900–911, Nov. 2012.
- [6] Y. Feng, X. Zhang, P. Graves, and Y. Zeng, “A comprehensive analysis of precursor microRNA cleavage by human Dicer,” *RNA*, vol. 18, no. 11, pp. 2083–2092, Nov. 2012.
- [7] I. J. MacRae, K. Zhou, and J. A. Doudna, “Structural determinants of RNA recognition and cleavage by Dicer,” *Nature Structural Mol. Biol.*, vol. 14, no. 10, pp. 934–940, Oct. 2007.
- [8] F. Ahmed, R. Kaundal, and G. P. Raghava, “PHDcleav: A SVM based method for predicting human Dicer cleavage sites using sequence and secondary structure of miRNA precursors,” *BMC Bioinf.*, vol. 14, no. S14, p. 9, Oct. 2013.
- [9] Y. Bao, M. Hayashida, and T. Akutsu, “LBSSizeCleav: Improved support vector machine (SVM)-based prediction of Dicer cleavage sites using loop/bulge length,” *BMC Bioinf.*, vol. 17, no. 1, p. 487, Nov. 2016.
- [10] P. Liu, J. Song, C.-Y. Lin, and T. Akutsu, “ReCGBM: A gradient boosting-based method for predicting human Dicer cleavage sites,” *BMC Bioinf.*, vol. 22, no. 1, p. 63, Feb. 2021.
- [11] L. Mu, J. Song, T. Akutsu, and T. Mori, “DiCleave: A deep learning model for predicting human Dicer cleavage sites,” *BMC Bioinf.*, vol. 25, no. 1, p. 13, Jan. 2024.
- [12] L. Mu and T. Akutsu, “DiCleavePlus : A transformer-based model to detect human dicer cleavage sites within cleavage patterns,” *Genes Cells*, vol. 31, no. 1, p. 70074, Jan. 2026.
- [13] S. Griffiths-Jones, H. K. Saini, S. van Dongen, and A. J. Enright, “MiRBase: Tools for microRNA genomics,” *Nucleic Acids Res.*, vol. 36, pp. D154–D158, Dec. 2007.
- [14] T. Xu, N. Su, L. Liu, J. Zhang, H. Wang, W. Zhang, J. Gui, K. Yu, J. Li, and T. D. Le, “MiRBaseConverter: An R/bioconductor package for converting and retrieving miRNA name, accession, sequence and family information in different versions of miRBase,” *BMC Bioinf.*, vol. 19, no. S19, p. 514, Dec. 2018.
- [15] M. J. Zvelebil, J. O. Baum, and M. Zvelebil, *Understanding Bioinformatics*. New York, NY, USA: Garland Science, 2008.
- [16] R. Lorenz, S. H. Bernhart, C. Höner zu Siederdissen, H. Tafer, C. Flamm, P. F. Stadler, and I. L. Hofacker, “ViennaRNA package 2.0,” *Algorithms for Mol. Biol.*, vol. 6, no. 1, p. 26, Nov. 2011.
- [17] C. C. Aggarwal, *Data Mining: The Textbook*. Cham, Switzerland: Springer, 2015.
- [18] G. Mendizabal-Ruiz, I. Román-Godínez, S. Torres-Ramos, R. A. Salido-Ruiz, and J. A. Morales, “On DNA numerical representations for genomic similarity computation,” *PLoS ONE*, vol. 12, no. 3, Mar. 2017, Art. no. e0173288.
- [19] D. Anastassiou, “Genomic signal processing,” *IEEE Signal Process. Mag.*, vol. 18, no. 4, pp. 8–20, Jul. 2001.
- [20] T. Rakthanmanon, B. Campana, A. Mueen, G. Batista, B. Westover, Q. Zhu, J. Zakaria, and E. Keogh, “Searching and mining trillions of time series subsequences under dynamic time warping,” in *Proc. 18th ACM SIGKDD Int. Conf. Knowl. Discovery Data Mining*, Aug. 2012, pp. 262–270.
- [21] P. D. Cristea, “Conversion of nucleotides sequences into genomic signals,” *J. Cellular Mol. Med.*, vol. 6, no. 2, pp. 279–303, Apr. 2002.
- [22] N. Chakravarthy, A. Spanias, L. D. Iasemidis, and K. Tsakalis, “Autoregressive modeling and feature analysis of DNA sequences,” *EURASIP J. Adv. Signal Process.*, vol. 2004, no. 1, pp. 1–16, Jan. 2004.
- [23] J. Zhao, X. W. Yang, J. P. Li, and Y. Y. Tang, “DNA sequences classification based on wavelet packet analysis,” in *Wavelet Analysis and its Applications*. Berlin, Germany: Springer, 2001, pp. 424–429.
- [24] T. Holden, R. Subramaniam, R. M. Sullivan, E. Cheung, C. Schneider, G. Tremberger, A. I. Flamholz, D. Lieberman, and T. Cheung, “ATCG nucleotide fluctuation of deinococcus radiodurans radiation genes,” *Proc. SPIE*, vol. 6694, Oct. 2007, Art. no. 669417.
- [25] A. S. Nair and S. P. Sreenadh, “A coding measure scheme employing electron-ion interaction pseudopotential (EIIP),” *Bioinformation*, vol. 1, pp. 197–202, Oct. 2006.
- [26] M. Akhtar, J. Epps, and E. Ambikairajah, “On DNA numerical representations for period-3 based exon prediction,” in *Proc. IEEE Int. Workshop Genomic Signal Process. Statist.*, Jun. 2007, pp. 1–4.
- [27] R. Zhang and C.-T. Zhang, “Z curves, an intuitive tool for visualizing and analyzing the DNA sequences,” *J. Biomolecular Struct. Dyn.*, vol. 11, no. 4, pp. 767–782, Feb. 1994.
- [28] J. A. Berger, S. K. Mitra, M. Carli, and A. Neri, “Visualization and analysis of DNA sequences using DNA walks,” *J. Franklin Inst.*, vol. 341, nos. 1–2, pp. 37–53, Jan. 2004.
- [29] A. Bagnall, J. Lines, A. Bostrom, J. Large, and E. Keogh, “The great time series classification bake off: A review and experimental evaluation of recent algorithmic advances,” *Data Mining Knowl. Discovery*, vol. 31, no. 3, pp. 606–660, May 2017.
- [30] A. P. Ruiz, M. Flynn, J. Large, M. Middlehurst, and A. Bagnall, “The great multivariate time series classification bake off: A review and experimental evaluation of recent algorithmic advances,” *Data Mining Knowl. Discovery*, vol. 35, no. 2, pp. 401–449, Mar. 2021.
- [31] M. Middlehurst, P. Schäfer, and A. Bagnall, “Bake off redux: A review and experimental evaluation of recent time series classification algorithms,” *Data Mining Knowl. Discovery*, vol. 38, no. 4, pp. 1958–2031, Jul. 2024.
- [32] A. Dempster, F. Petitjean, and G. I. Webb, “ROCKET: Exceptionally fast and accurate time series classification using random convolutional kernels,” *Data Mining Knowl. Discovery*, vol. 34, no. 5, pp. 1454–1495, Sep. 2020.
- [33] A. Dempster, D. F. Schmidt, and G. I. Webb, “MiniRocket: A very fast (Almost) deterministic transform for time series classification,” in *Proc. 27th ACM SIGKDD Conf. Knowl. Discovery Data Mining*, New York, NY, USA, Aug. 2021, pp. 248–257.
- [34] C. W. Tan, A. Dempster, C. Bergmeir, and G. I. Webb, “MultiRocket: Multiple pooling operators and transformations for fast and effective time series classification,” *Data Mining Knowl. Discovery*, vol. 36, no. 5, pp. 1623–1646, Sep. 2022.
- [35] A. Dempster, D. F. Schmidt, and G. I. Webb, “Hydra: Competing convolutional kernels for fast and accurate time series classification,” *Data Mining Knowl. Discovery*, vol. 37, no. 5, pp. 1779–1805, Sep. 2023.
- [36] B. W. Matthews, “Comparison of the predicted and observed secondary structure of T4 phage lysozyme,” *Biochimica et Biophysica Acta (BBA)-Protein Struct.*, vol. 405, no. 2, pp. 442–451, Oct. 1975.
- [37] J. Gorodkin, “Comparing two K-category assignments by a K-category correlation coefficient,” *Comput. Biol. Chem.*, vol. 28, no. 5, pp. 367–374, Dec. 2004.

956
957
958
959
960
961
962
963
964
965
966
967

COLEMAN YU received the B.Sc. degree in pure physics, with minor programs in mathematics, and information technology, in 2014, and the M.Phil. degree in technology leadership and entrepreneurship from the Department of Computer Science and Engineering, The Hong Kong University of Science and Technology, in 2016. He is currently pursuing the Ph.D. degree in informatics with the Bioinformatics Center, Institute for Chemical Research, Kyoto University.

His research interests include data mining, particularly in time series, and bioinformatics.

968
969
970
971
972
973
974
975
976
977
978
979
980
981
982
983

RAYMOND CHI-WING WONG received the B.Sc., M.Phil., and Ph.D. degrees in computer science and engineering from The Chinese University of Hong Kong (CUHK), in 2002, 2004, and 2008, respectively. From 2004 to 2005, he was a Research and Development Assistant under a research and development project funded by ITF and a local industrial company called Lifewood. He was the Associate Director of the Computer Engineering (CPEG) Program, from 2012 to 2014, the Director of the Computer Engineering (CPEG) Program, from 2014 to 2016, the Director of the Risk Management and Business Intelligence (RMBI) Program, from 2017 to 2019, and the Associate Director of the Data Science and Technology (DSCT) Program, from 2019 to 2021. He is currently a Professor in computer science and engineering (CSE) with The Hong Kong University of Science and

Technology (HKUST). He is the Associate Head of the Department of Computer Science and Engineering (CSE) and the Director of the Undergraduate Research Opportunities Program (UROP). He published 135 conference papers (e.g., SIGMOD, SIGKDD, VLDB, ICDE, and ICDM), 50 journal/chapter papers (e.g., TODS, DAMI, TKDE, VLDB journal, and TKDD), and one book. He reviewed papers from conferences and journals related to data mining and database, including VLDB conference, SIGMOD, TODS, VLDB journal, TKDE, TKDD, ICDE, SIGKDD, ICDM, DAMI, DaWaK, PAKDD, EDBT, and IJDMW. His research interests include database and data mining. He is a Program Committee Member of conferences, including SIGMOD, VLDB, ICDE, KDD, ICDM, and SDM, and a referee of journals, including TODS, VLDBJ, TKDE, TKDD, DAMI, and KAIS. He received 43 Awards.

984
985
986
987
988
989
990
991
992
993
994
995
996
997
998
999
1000
1001
1002
1003
1004
1005
1006
1007

TATSUYA AKUTSU (Senior Member, IEEE) received the B.E. and M.E. degrees in aeronautics and the D.E. degree in information engineering from The University of Tokyo, 1984, 1986, and 1989, respectively. He has been a Professor with the Bioinformatics Center, Institute for Chemical Research, Kyoto University, since 2001. His research interests include bioinformatics, complex networks, neural networks, and discrete algorithms.

• • •